



# Metallic AgInS<sub>2</sub> nanocrystals with sulfur vacancies boost atmospheric CO<sub>2</sub> photoreduction under near-infrared light illumination

Kai Wang<sup>a</sup>, Haotian Qin<sup>a</sup>, Jun Li<sup>b,\*</sup>, Qiang Cheng<sup>a</sup>, Yanfang Zhu<sup>c</sup>, Haiyan Hu<sup>c</sup>, Jian Peng<sup>c</sup>, Shuangqiang Chen<sup>d,\*</sup>, Guohong Wang<sup>a</sup>, Shulei Chou<sup>c</sup>, Shixue Dou<sup>e</sup>, Yao Xiao<sup>c,f,\*\*</sup>

<sup>a</sup> College of Urban and Environmental Sciences, Hubei Key Laboratory of Pollutant Analysis and Reuse Technology, Huangshi Key Laboratory of Prevention and Control of Soil Pollution, Hubei Normal University, Huangshi 435002, PR China

<sup>b</sup> Henan Institute of Advanced Technology, Zhengzhou University, Zhengzhou 450052, PR China

<sup>c</sup> Institute for Carbon Neutralization, College of Chemistry and Materials Engineering, Wenzhou University, Wenzhou 325035, PR China

<sup>d</sup> Department of Chemical Engineering, School of Environmental and Chemical Engineering, Shanghai University, Shanghai 200444, PR China

<sup>e</sup> Institute of Energy Materials Science (IEMS), University of Shanghai for Science and Technology, Shanghai 200093, PR China

<sup>f</sup> State Key Laboratory of Electrical Insulation and Power Equipment, School of Electrical Engineering, Xi'an Jiaotong University, Xi'an 710049, PR China

## ARTICLE INFO

### Keywords:

Vacancy

AgInS<sub>2</sub>

Metallic catalyst

CO<sub>2</sub> photoreduction

Near-infrared light

## ABSTRACT

Unraveling the function of vacancy engineering in influencing the intrinsic CO<sub>2</sub> photoreduction with low photon energy directly from air remains a significant challenge. Here, a metallic photocatalyst, ultrafine AgInS<sub>2</sub> nanocrystals with sulfur vacancies (V<sub>S</sub>-AgInS<sub>2</sub>) is designed to exhibit superior atmospheric CO<sub>2</sub> reduction performance under near-infrared (NIR) light. Theoretical calculations reveal that the presence of sulfur vacancies and metallic characteristics result in extended spectrum absorption to the NIR region and efficient separation of charge carriers. As evidenced by *In situ* Diffuse Reflectance Infrared Fourier Transform Spectroscopy (DRIFTS) experiment and theoretical calculations, the unique properties of charge delocalization around the vacancy-induced dual sites at AgInS<sub>2</sub> nanocrystals contribute to COOH\* intermediates for CO production while simultaneously inhibiting the formation of CHO\* intermediates. Consequently, the metallic V<sub>S</sub>-AgInS<sub>2</sub> nanocrystals demonstrate nearly 100% selective CO production with a rate of 8.04 μmol g<sup>-1</sup> h<sup>-1</sup> under NIR irradiation, even directly from atmospheric CO<sub>2</sub> in the air.

## 1. Introduction

Artificial photosynthesis systems can directly convert solar energy, carbon oxide, and water into hydrocarbons and oxygen, thus providing a promising pathway to address the energy crisis and greenhouse effect, and ultimately achieve carbon neutralization [1–4]. However, photocatalytic CO<sub>2</sub> reduction reactions (RR) are still far from suitable for practical applications due to poor thermodynamic stability and low quantum efficiencies [5–7]. Previously reported semiconductor-based photocatalysts typically possess wide bandgap, limiting spectrum absorption to visible light region, while the near-infrared (NIR) light, accounting for approximately 50% of the solar spectrum, is incompatible with most photocatalyst systems [8–12]. Additionally, the rapid electron-hole recombination in photocatalysts and the high activation energy barrier in CO<sub>2</sub> RR further hinder the development of NIR

light-responsive CO<sub>2</sub> RR [13–16]. As a result, exploring novel material systems with NIR light absorption, tunable carrier mobility, and intrinsic large carrier density is essential for achieving ideal CO<sub>2</sub> RR performance under NIR light illumination.

Although several photocatalyst systems, such as metal oxides, nitrides, and polymers have been reported as candidates for photocatalytic CO<sub>2</sub> RR—they usually undergo photo-corrosion under solar irradiation [17–22]. In contrast, metal sulfide-based semiconductor photocatalysts are generally more thermodynamically stable, thus making them appropriate candidates for CO<sub>2</sub> RR [23–27]. Among them, novel ternary metal chalcogenides have emerged as promising candidates for wide-spectrum responsive CO<sub>2</sub> reduction due to their suitable conduction band potential and tunable band gap [28–31]. Despite these advantages, pristine ternary metal chalcogenides typically suffer from low CO<sub>2</sub> photoconversion efficiency, primarily attributed to limited NIR

\* Corresponding authors.

\*\* Corresponding author at: Institute for Carbon Neutralization, College of Chemistry and Materials Engineering, Wenzhou University, Wenzhou 325035, PR China.

E-mail addresses: [junli2019@zju.edu.cn](mailto:junli2019@zju.edu.cn) (J. Li), [chensq@shu.edu.cn](mailto:chensq@shu.edu.cn) (S. Chen), [xiaoyao@wzu.edu.cn](mailto:xiaoyao@wzu.edu.cn) (Y. Xiao).

<https://doi.org/10.1016/j.apcatb.2023.122763>

Received 2 January 2023; Received in revised form 4 April 2023; Accepted 11 April 2023

Available online 12 April 2023

0926-3373/© 2023 Elsevier B.V. All rights reserved.

light absorption, a very low density of coordinated surface-active sites, and intrinsically poor electrical conductivity.

Interestingly, vacancy-rich semiconductor photocatalysts appear to be the most promising materials for wide-spectrum visible light-responsive photoredox reactions, owing to their adjusted bandgap, tunable carrier mobility, and high density of exposed surface-active sites [32–34]. The introduction of vacancies can create new defect levels and tailor the band structure, potentially acting as inter-band energy levels to accept photogenerated carriers and further extend spectrum absorption toward the NIR region [35–37]. Moreover, the presence of vacancies may tune the charge density distribution, reducing the activation energy barrier of CO<sub>2</sub> RR and stabilizing the intermediates of CO<sub>2</sub> photoreduction [38–41]. Furthermore, vacancy-induced photocatalysts possess higher carrier concentration and electric conductivity than conventional semiconductors. The small bandgaps induced by surface defects endow the metallic photocatalysts with highly efficient solar spectrum harvesting, especially in the NIR region, which is considered one of the prerequisites for achieving NIR light driven CO<sub>2</sub> RR. Therefore, engineering surface defects in ternary metal chalcogenides as a metallic photocatalyst is a significant path to realizing high-efficiency photocatalytic CO<sub>2</sub> RR under NIR light.

As a proof-of-concept demonstration, ultrafine AgInS<sub>2</sub> nanocrystals are selected as the ideal photocatalyst system for investigation [42–45]. We first fabricate sulfur-vacancy modified AgInS<sub>2</sub> (V<sub>S</sub>-AgInS<sub>2</sub>) nanocrystals, wherein temperature-dependent resistivities, electron spin resonance (ESR), UV–vis–NIR DRS spectra, combined with density functional theory (DFT) study reveal that the sulfur vacancy-induced metallic nature is suitable for NIR light-triggered CO<sub>2</sub> RR. Femtosecond transient absorption spectroscopy (fs-TAS) under NIR-light unveils that the vacancy-rich surface of AgInS<sub>2</sub> nanocrystals significantly reduces the recombination of photogenerated electron-hole pairs. As such, the ultrathin AgInS<sub>2</sub> nanocrystals with a sulfur vacancy can implement NIR light-driven CO<sub>2</sub> RR, achieving a boosted CO formation rate of 8.04 μmol g<sup>−1</sup> h<sup>−1</sup> with remarkably high selectivity and reaching nearly 100% of selectivity in atmospheric CO<sub>2</sub>.

## 2. Materials and methods

### 2.1. Photocatalyst preparation

**Synthesis of AgInS<sub>2</sub> nanocrystal:** First, 0.2 mmol of AgNO<sub>3</sub>, 0.2 mmol of In(NO<sub>3</sub>)<sub>3</sub>·4 H<sub>2</sub>O, and 4 mmol of thioacetamide (TAA) were mixed with 60 mL of deionized (DI) water under vigorous stirring. The mixed solution was then transferred into 100 mL Teflon-lined autoclaves, which were sealed and kept at 180 °C for 24 h before being allowed to cool down naturally. The precipitate was filtered, washed three times, and then dried overnight at 70 °C.

**Synthesis of V<sub>S</sub>-AgInS<sub>2</sub> nanocrystal:** The as-obtained AgInS<sub>2</sub> nanocrystals were rapidly heated at 400 °C for 75 s in Ar with H<sub>2</sub>/Ar. The sample was removed from the tube furnace immediately after the rapid heating process and then cooled in liquid nitrogen.

### 2.2. Characterization

The physical and chemical properties of the catalysts were characterized by XRD, SEM, TEM, Raman, FT-IR, ESR, BET, UV–vis–NIR DRS, XPS, TPD, SPV, fs-TAS, and in situ DRIFTS. The contents of characterization are described in Text S1 of the [supplementary materials](#).

### 2.3. DFT calculation

DFT calculations were performed in the Vienna ab initio simulation package (VASP). The details of the calculation methodology are shown in Text S2 of the [supplementary materials](#).

### 2.4. Photocatalytic CO<sub>2</sub> reduction reaction

The photocatalyst (20 mg) was placed onto the bottom of a photochemistry reactor (PQ253, Beijing Perfectlight), and then 500 μL of deionized (DI) water was injected onto the surface of the catalyst. High-purity CO<sub>2</sub> (99.999%) and low-concentration CO<sub>2</sub> (nitrogen equilibrium gas and 1000 ppm CO<sub>2</sub>, nitrogen equilibrium gas and 500 ppm CO<sub>2</sub>, and fresh air) served as the CO<sub>2</sub> sources for the photocatalytic reactions. Each set of experiments was irradiated by xenon (Xe) lamp (PLS-SXE300D, Beijing Perfectlight) with cut-off filters (UVCUT 400, CUT800, Beijing Perfectlight). Moreover, the gas products were qualitatively analyzed by an online gas chromatography system (Labsolar-6A, Beijing Perfectlight) with a cooling water system and a gas chromatograph (GC2014C, Shimadzu) equipped with flame ionization detection (FID) and thermal conductivity detection (TCD). Furthermore, the <sup>13</sup>C-labeled products were analyzed by 6890 N/5975 (Agilent, United States of America) gas chromatography-mass spectrometry (GC-MS). The apparent quantum yield (AQY) was measured using a 300 W Xenon lamp (PLS-SXE300, Perfectlight, China) with bandpass filters of 710, 790, 850, 920, and 1050 nm. The AQY was calculated by Equation:  $AQY(\%) = \frac{CO\ molecules + 2 \times CH_4\ molecules}{incident\ photons} \times 100\%$ .

### 2.5. Photoelectrochemical tests

Details about the photoelectrochemical methodology are shown in Text S3 of the [supplementary materials](#).

## 3. Results and discussion

### 3.1. Morphological and structural characterizations

AgInS<sub>2</sub> is a ternary metal chalcogenide with wide spectrum harvesting ability and durable, non-toxic properties, suggesting that it could be capable of photocatalytic CO<sub>2</sub> RR. Because of its unique electronic properties and exposed metal sites, it is reasonable to infer that AgInS<sub>2</sub> should be a promising catalyst with anionic vacancy to manipulate product selectivity in CO<sub>2</sub> RR under NIR light illumination. As such, we first fabricated pristine AgInS<sub>2</sub> nanocrystals (Fig. S1), and then we purposely introduced surface sulfur vacancies (V<sub>S</sub>-AgInS<sub>2</sub>) using an ultrafast calcination process (Fig. S2). The X-ray diffraction (XRD) patterns for the obtained AgInS<sub>2</sub> and V<sub>S</sub>-AgInS<sub>2</sub> nanocrystals (Fig. S3) can be indexed to tetragonal AgInS<sub>2</sub> nanocrystal (JCPDS No. 25–1330), which illustrates that the ultrafast calcination process has no influence on the structure of AgInS<sub>2</sub> nanocrystals. The field emission scanning electron microscopy (FESEM) images of the two samples display a similar sheet-like morphology (Figs. S4–5), and the TEM image of AgInS<sub>2</sub> nanocrystals exhibit the stable triangle-shape morphology in Fig. 1a. Meanwhile, the HRTEM image in Fig. 1b exhibits a high degree of orientation along the [112] direction. In addition, regional lattice disorder is also observed inside the red square [10]. High-angle annular dark field (HAADF) scanning TEM image and elemental mappings displayed in Fig. 1c verify the homogeneous distribution of Ag (blue), In (green), and S (red) elements.

Fig. 1d shows the Raman spectra of the AgInS<sub>2</sub> and V<sub>S</sub>-AgInS<sub>2</sub> nanocrystals. Four Raman peaks at 217, 282, 322, and 471 cm<sup>−1</sup> can be assigned to the E(L)/B<sub>2</sub>(L), A<sub>1</sub>, E(L), and E(L)/B<sub>2</sub>(L) modes in AgInS<sub>2</sub> nanocrystal [44]. After the rapid heat treatment, the intensities of V<sub>S</sub>-AgInS<sub>2</sub> are lower than AgInS<sub>2</sub>, and the decreased thickness and vacancies could induce the disappearance of some characteristic peaks. This phenomenon is similar to some reported vacancy-rich photocatalysts, such as CuS, NiAl-LDH, and Bi<sub>12</sub>O<sub>17</sub>C<sub>12</sub> [17,28,33]. Remarkably, the S 2p XPS peak of V<sub>S</sub>-AgInS<sub>2</sub> exhibits a 0.22 eV positive shift relative to that of pristine AgInS<sub>2</sub> nanocrystals (Fig. 1e), while their Ag 3d and In 3d XPS peaks show the negative shift (Fig. S6) [46,47]. Besides, the FT-IR spectra of AgInS<sub>2</sub>, V<sub>S</sub>-AgInS<sub>2</sub>, and TAA were displayed in

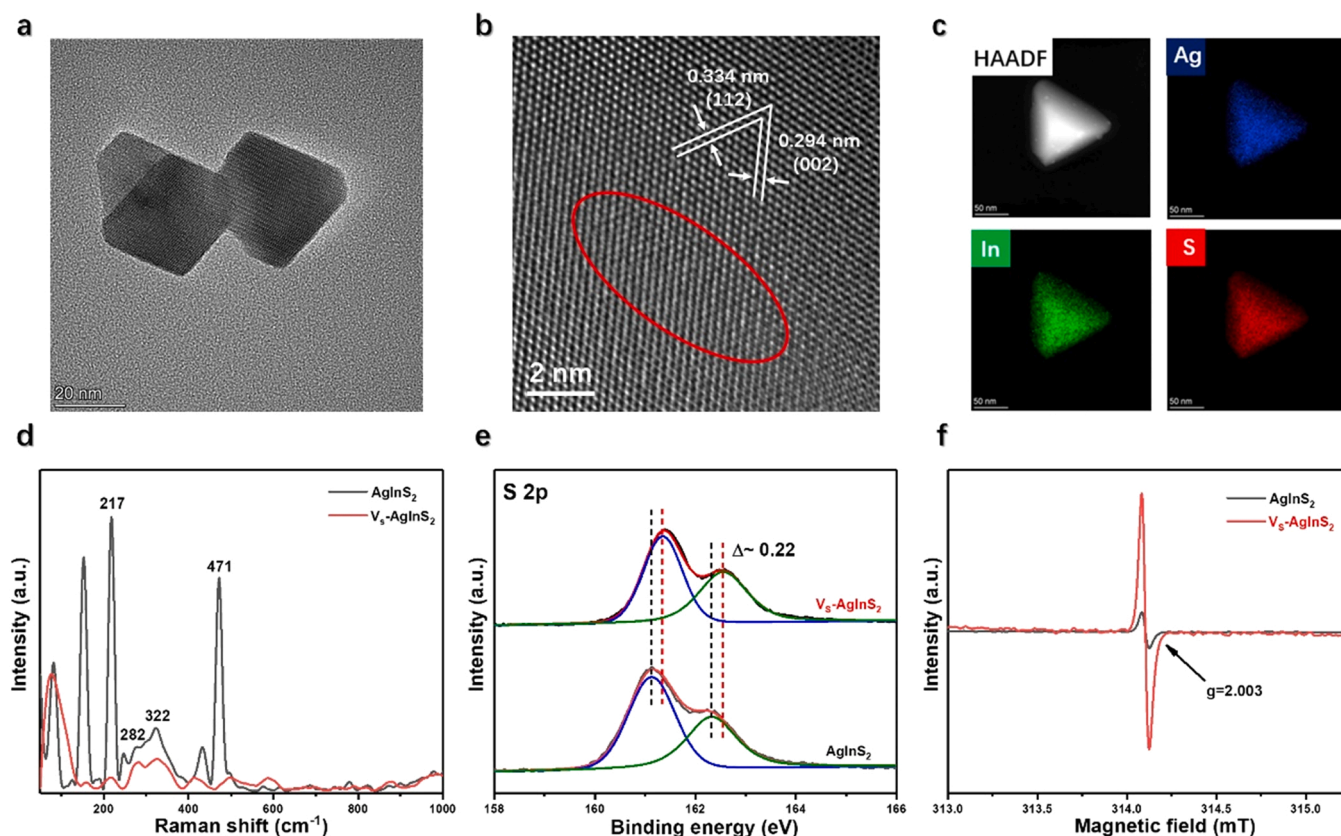


**Fig. 1.** (a) TEM, (b) HRTEM and (c) HAADF-STEM image and corresponding EDX mapping images of  $V_S$ -AgInS<sub>2</sub> nanocrystals. (d) Raman spectra, (e) S 2p XPS spectra and (f) EPR signals of AgInS<sub>2</sub> and  $V_S$ -AgInS<sub>2</sub> nanocrystals.

**Fig. S7.** The peaks below 1700  $\text{cm}^{-1}$  were assigned to the C-H, C-C, and C-S stretching vibrations. The weaker peaks below 3000  $\text{cm}^{-1}$  in  $V_S$ -AgInS<sub>2</sub> confirm the lower content of H-S bonds due to the sulfur vacancy [43,44]. The higher binding energy of S with Ag and In in  $V_S$ -AgInS<sub>2</sub> results from the deficiency of S in the crystal structure, which again proves the existence of S vacancy sites. In addition, the presence of a higher concentration of sulfur vacancies in  $V_S$ -AgInS<sub>2</sub> can be further evidenced by the enhanced ESR signal at  $g = 2.003$  (Fig. 1f).

As shown in Fig. 2a, the calculated density of states (DOS) of  $V_S$ -AgInS<sub>2</sub> extends over the Fermi level (0 eV), predicting its metallic nature. Meanwhile, the results of valence-band XPS measurements (Fig. 2b) confirm that there is an overlap between the valence band maximum and the Fermi level, which again verifies the metallicity of  $V_S$ -AgInS<sub>2</sub> [48]. In addition, the calculated band structure in Fig. 2c also implies a typical metallic band structure, consisting of the lowest unoccupied band ( $B_1$ ), the partially occupied band (CB), and the highest fully occupied band ( $B_{-1}$ ). Moreover, for  $V_S$ -AgInS<sub>2</sub>, the observed increase in resistance with temperature ranging from 160 to 300 K unambiguously affirms its metallic characteristics (Fig. 2d). Explicitly, the metallic characteristics of  $V_S$ -AgInS<sub>2</sub> can be attributed to the existence of sulfur vacancies.

At the same time, the sulfur vacancies introduce some inter-band defect energy levels, which allow photogenerated charge carriers to reside. However, for pristine AgInS<sub>2</sub>, a conventional semiconductor type band structure can be expected. Consequently, apparently enhanced light harvesting performance, especially in the NIR range, is obtained for the  $V_S$ -AgInS<sub>2</sub> sample, while the pristine AgInS<sub>2</sub> sample only responds to visible light up to 700 nm (Fig. 2e). The energy gaps ( $E_g$ ) of pristine AgInS<sub>2</sub> and  $V_S$ -AgInS<sub>2</sub> were determined to be 1.80 and 1.71 eV, respectively (Fig. S8). As displayed in Fig. S9, valence-band XPS measurements gave the VB positions of pristine AgInS<sub>2</sub> and  $V_S$ -AgInS<sub>2</sub>. Therefore, the electronic band structures for AgInS<sub>2</sub> and  $V_S$ -AgInS<sub>2</sub> were

obtained in Fig. S10.  $V_S$ -AgInS<sub>2</sub> generated free charge carriers through intra-band transition (transitions in CB from the lower level to  $E_F$ ) and inter-band transition (transitions from  $E_F$  to  $B_1$ ) even under NIR light illumination (Fig. 2f). The electrons in  $B_1$  could convert CO<sub>2</sub> to solar fuels due to the more negative position.

### 3.2. CO<sub>2</sub> photoreduction performances

To evaluate the NIR light photoactivity, CO<sub>2</sub> RR experiments are conducted using an Xe lamp ( $> 780$  nm) as a light source. As shown in Fig. 3a, in the dark, no detectable CO production is obtained for both AgInS<sub>2</sub> and metallic  $V_S$ -AgInS<sub>2</sub> nanocrystals. Meanwhile, under NIR light irradiation, only trace CO generation can be detected for AgInS<sub>2</sub>. In contrast, the metallic  $V_S$ -AgInS<sub>2</sub> nanocrystals exhibit outstanding CO<sub>2</sub> RR performance under NIR light irradiation. As shown in Fig. 3a, the CO evolution rate of the  $V_S$ -AgInS<sub>2</sub> reaches  $8.04 \mu\text{mol g}^{-1} \text{h}^{-1}$ , which is about 81 times higher than that of the AgInS<sub>2</sub>. Interestingly, as an oxidation product, a significant amount of O<sub>2</sub> can also be detected for the metallic  $V_S$ -AgInS<sub>2</sub>, while still a trace amount of O<sub>2</sub> is observed for AgInS<sub>2</sub>, manifesting the excellent NIR photoactivity of  $V_S$ -AgInS<sub>2</sub>. Moreover, the dependence of photocatalytic CO<sub>2</sub> RR properties on light sources of the samples is evaluated (Fig. 3b, S11; control experiments in Fig. S12). Under full spectrum light (UV-vis-NIR) and visible light irradiation, for metallic  $V_S$ -AgInS<sub>2</sub> nanocrystals, the main reduction product is CO accompanied by a small amount of CH<sub>4</sub>, indicating good selectivity. Moreover, high-resolution thermographic photographs in Fig. S13 clearly show that the full spectrum and NIR light irradiation (3 h) on the pristine AgInS<sub>2</sub> and  $V_S$ -AgInS<sub>2</sub> only caused a slight change, implying that NIR light illumination could be realized at ambient temperatures with the assistance of circulating water, further exclude the influence of photo-thermal effect [28]. For pristine AgInS<sub>2</sub>, the evolution rates of CO and CH<sub>4</sub> are comparable. It is clear that, in the NIR



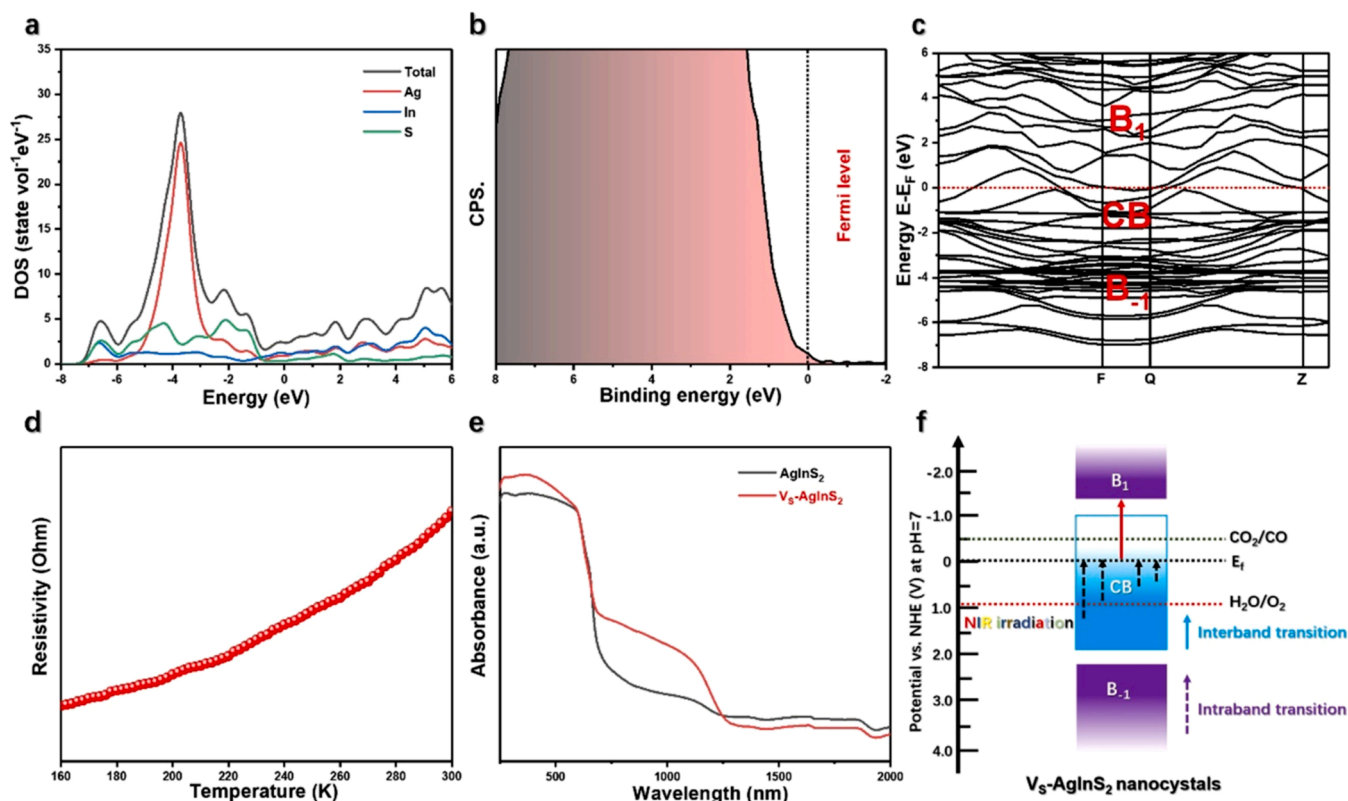


**Fig. 2.** (a) Calculated density of states, (b) valence band XPS spectrum and (c) calculated band structure of  $V_5\text{-AgInS}_2$ . (d) Temperature-dependent resistivities of  $V_5\text{-AgInS}_2$  nanocrystals. (e) UV-vis-NIR diffuse reflectance spectra of  $\text{AgInS}_2$  and  $V_5\text{-AgInS}_2$  nanocrystals. (f) Schematics illustrating the photon transition processes in the metallic  $V_5\text{-AgInS}_2$  nanocrystals.

region, the metallic  $V_5\text{-AgInS}_2$  nanocrystals possess much higher photocatalytic activity for  $\text{CO}_2$  RR than pristine  $\text{AgInS}_2$ , and even outperform some reported photocatalysts under NIR light irradiation (Table S1), such as  $\text{Rb}_{0.33}\text{WO}_3$ ,  $\text{O}_V\text{-WO}_3$  and  $\text{Bi}_{19}\text{Br}_3\text{S}_{27}$ .

Furthermore, from Fig. 3c, it is clear that the metallic  $V_5\text{-AgInS}_2$  catalyst exhibits a gradual upward trend towards CO generation in different concentrations of  $\text{CO}_2$ , such as 1000 ppm of  $\text{CO}_2$ , 500 ppm in simulated  $\text{CO}_2$ , even directly from air under NIR light irradiation. Noteworthy, the fresh air containing atmospheric  $\text{CO}_2$  was directly used as the carbon source. The results in Fig. S14 confirmed the TAA was not acting as the hole-sacrificing agent but restrained the photocatalytic  $\text{CO}_2$  RR under full spectrum and NIR light illumination. More importantly, the NIR light  $\text{CO}_2$  reduction activities for the metallic  $V_5\text{-AgInS}_2$  show no obvious decay after five cycles, which is up to 20 h successive photocatalytic reaction (Fig. 3d and S15), indicating its exceptional photocatalytic stability. Besides, the apparent quantum efficiency (AQY) test in the range of 700–1100 nm is also performed, and the results are shown in Fig. 3e. Clearly, the pristine  $\text{AgInS}_2$  nanocrystals exhibit negligible AQY (%). In contrast, at 790 nm, the metallic  $V_5\text{-AgInS}_2$  nanocrystals exhibit a quantum efficiency of 0.055%, which is much higher than that of the pristine  $\text{AgInS}_2$ . Notably, the preponderance in AQY (%) of metallic  $V_5\text{-AgInS}_2$  is maintained even up to 1050 nm, denoting the high photoelectric conversion efficiency, which is critical for the high performance NIR photocatalytic reaction. To determine the origin of CO, isotope-labeled carbon dioxide ( $^{13}\text{CO}_2$ ) reduction over metallic  $V_5\text{-AgInS}_2$  nanocrystals is performed. From Fig. 3f, the signal at  $m/z = 29$  corresponds to  $^{13}\text{CO}$ , and the others ( $^{13}\text{C}$  at  $m/z = 13$  and  $^{16}\text{O}$  at  $m/z = 16$ ) are assigned to the signals of  $^{13}\text{CO}$ , confirming that the CO generation originated from the  $\text{CO}_2$  photoreduction. Additionally, the  $V_5\text{-AgInS}_2$  nanocrystals could achieve water oxidation to form  $\text{O}_2$  as further verified by an  $\text{H}_2^{18}\text{O}$  labeling experiment (Fig. S16).

Next, in situ Diffuse Reflectance Infrared Fourier Transform

Spectroscopy (in situ DRIFTS) measurements were performed to probe the reaction mechanism of the photocatalytic  $\text{CO}_2$  RR over the  $V_5\text{-AgInS}_2$ . The absorption peak at 1635, 1631, and 1648  $\text{cm}^{-1}$  might be attributed to  $^*\text{CO}_2$  under full spectrum light with pure  $\text{CO}_2$ , full spectrum light with air, and NIR light with air, respectively. Under full spectrum light irradiation, the peaks at about 1308, 1332  $\text{cm}^{-1}$  are assigned to the bidentate carbonate ( $\text{b-CO}_3^{2-}$ ) over pristine  $\text{AgInS}_2$  and  $V_5\text{-AgInS}_2$ , respectively (Fig. 3g and S17). The peaks at around 1430  $\text{cm}^{-1}$  correspond to  $^*\text{HCO}_3^-$ . An obvious absorption peak at around 1590  $\text{cm}^{-1}$  over pristine  $\text{AgInS}_2$  and  $V_5\text{-AgInS}_2$  (Fig. 3g–i and S17) emerges, resulting in  $^*\text{COOH}$ , which is a crucial intermediate for  $\text{CO}_2$  photoreduction to CO or  $\text{CH}_4$  [48]. As displayed in Fig. 3g–h, the absorption bands at 1173 and 1102  $\text{cm}^{-1}$  belong to the  $^*\text{CH}_3\text{O}$  group, which was an important intermediate for the generation of  $\text{CH}_4$ . Moreover, a sharp peak located at 1063  $\text{cm}^{-1}$  was assigned to the  $^*\text{CHO}$  group. As exhibited in Fig. 3g–i, the peaks of  $^*\text{CH}_3\text{O}$  and  $^*\text{CHO}$  groups disappeared, which illustrated the lack of production of  $\text{CH}_4$  in the air atmosphere. Further, the slight  $^*\text{CO}$  peak at around 2080  $\text{cm}^{-1}$  was clearly detected in pure  $\text{CO}_2$  atmosphere under both NIR light and full spectrum light irradiation, thus suggesting the weak  $^*\text{CO}$  adsorption and release of gaseous CO.

### 3.3. Photoelectrochemical properties and charge dynamics

As shown in Fig. 4a, photoelectrodes of pristine  $\text{AgInS}_2$  nanocrystals and metallic  $V_5\text{-AgInS}_2$  nanocrystals deposited on F-doped tin oxide (FTO) substrates exhibit repeatable photocurrent response under full spectrum irradiation with on/off cycles. Interestingly, a much higher current intensity in the  $V_5\text{-AgInS}_2$  photoelectrode is obtained, indicating its higher density of photogenerated charges. Under only NIR light irradiation (Fig. 4b), pristine  $\text{AgInS}_2$  nanocrystals show negligible photocurrent. In comparison, the metallic  $V_5\text{-AgInS}_2$  nanocrystals display strikingly enhanced photocurrent, which further confirms the

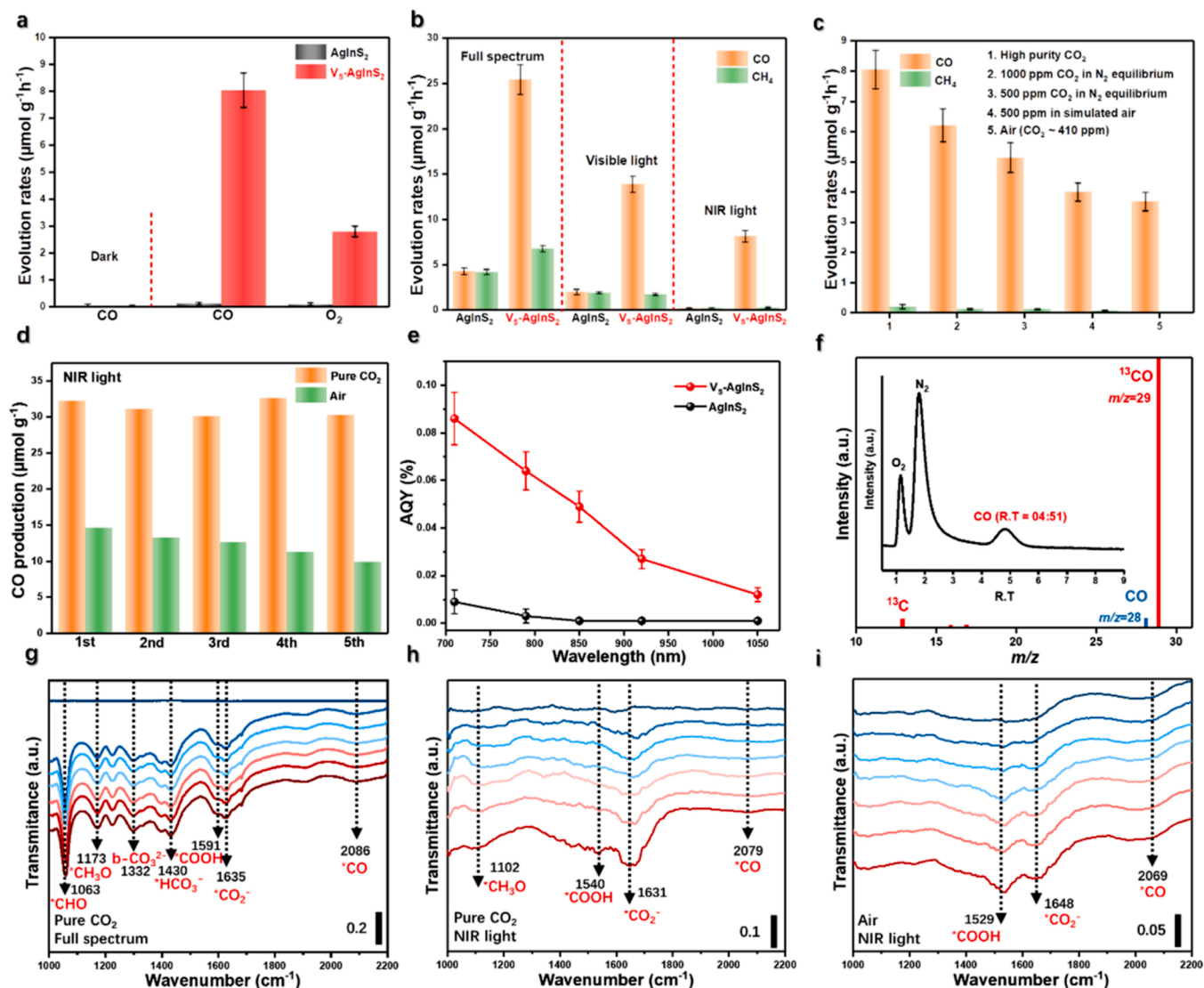


**Fig. 3.** (a) CO and O<sub>2</sub> production rates under NIR light irradiation as well as at 25 °C in the dark condition. Photocatalytic CO<sub>2</sub> RR (b) in pure CO<sub>2</sub>, (c) under different concentrations of CO<sub>2</sub>. (d) Cycling experiments of CO<sub>2</sub> RR under NIR light. (e) Wavelength-dependent AQY (%). (f) GC-MS spectra (inset of total ion chromatography) over V<sub>5</sub>-AgInS<sub>2</sub>. *In-situ* DRIFTS spectra of V<sub>5</sub>-AgInS<sub>2</sub> (g) under full spectrum irradiation, (h) under NIR light irradiation, and (i) in air.

excellent NIR responsivity of V<sub>5</sub>-AgInS<sub>2</sub>. Additionally, surface photovoltage spectroscopy (SPV) is employed to evaluate the aforementioned samples. As displayed in Fig. 4c, the metallic V<sub>5</sub>-AgInS<sub>2</sub> nanocrystals display significantly higher SPV signals and EIS plots (Fig. S19) relative to the pristine AgInS<sub>2</sub> nanocrystals. As displayed in Fig. 4d, the PL intensity of the V<sub>5</sub>-AgInS<sub>2</sub> decreases sharply in comparison with the AgInS<sub>2</sub>, which suggests that the carrier recombination rate is hindered effectively. The above results illustrate that sulfur vacancies can reduce the recombination rate of carriers in metallic V<sub>5</sub>-AgInS<sub>2</sub> nanocrystals and thereby improve the potential ability of photocatalytic CO<sub>2</sub> RR.

To further study the microscopic dynamic behaviors of photoinduced charge carriers in the prepared samples, femtosecond transient absorbance spectra (fs-TAS) of AgInS<sub>2</sub> and metallic V<sub>5</sub>-AgInS<sub>2</sub> nanocrystals in visible and NIR ranges are recorded (Figs. 4e and 4f). Notably, Figs. 4e and 4f show the multiple positive peaks in TA curves of V<sub>5</sub>-AgInS<sub>2</sub> (ca. 500 nm) and V<sub>5</sub>-AgInS<sub>2</sub> (ca. 550 nm) in the UV-vis region, which were ascribed to excited state absorption. In addition, a similar positive absorption peak above 800 nm was observed in both TAS signals of AgInS<sub>2</sub> in the NIR region (Fig. S19a). However, metallic V<sub>5</sub>-AgInS<sub>2</sub> exhibited a stronger absorption than AgInS<sub>2</sub> near 1200 nm (Fig. S19b), thus suggesting more efficient charge generation and separation. Figs. 4g and 4h

depict 2D TA mappings of AgInS<sub>2</sub> and metallic V<sub>5</sub>-AgInS<sub>2</sub> nanocrystals. Specifically, ground-state bleach (GSB), excited-state absorption (ESA), and stimulated emission (SE) signals are observed in the fs-TAS of both AgInS<sub>2</sub> and V<sub>5</sub>-AgInS<sub>2</sub> [48,49]. Moreover, the GSB and ESA signals of V<sub>5</sub>-AgInS<sub>2</sub> shift to the high wavelength in the presence of sulfur vacancy, which is coupled with the 2D TA mappings under NIR illumination (Fig. S20). For pristine AgInS<sub>2</sub>, the TA decay curve could be expressed by a biexponential function, in which  $\tau_1 = 5.47$  ps (62.2%),  $\tau_2 = 32.56$  ps (37.8%), and the average lifetime was 26.71 ps. However, the TA curve of V<sub>5</sub>-AgInS<sub>2</sub> could also be fitted by a biexponential decay function ( $\tau_1 = 6.36$  ps, 56.1%;  $\tau_2 = 32.56$  ps, 43.9%; average lifetime was 27.46 ps). The longer lifetime of V<sub>5</sub>-AgInS<sub>2</sub> might be due to its metallicity, resulting in the defect energy level created by sulfur vacancy can effectively suppressing the recombination of carriers. The inset in Fig. 4i depicted the possible electron relaxation processes over V<sub>5</sub>-AgInS<sub>2</sub>. The aforementioned analyses demonstrated the remarkable influence of sulfur vacancy on charge separation in metallic V<sub>5</sub>-AgInS<sub>2</sub> photocatalysts.

### 3.4. DFT study and photocatalytic mechanism

To unveil the interfacial catalysis reaction of CO<sub>2</sub> to CO, surface

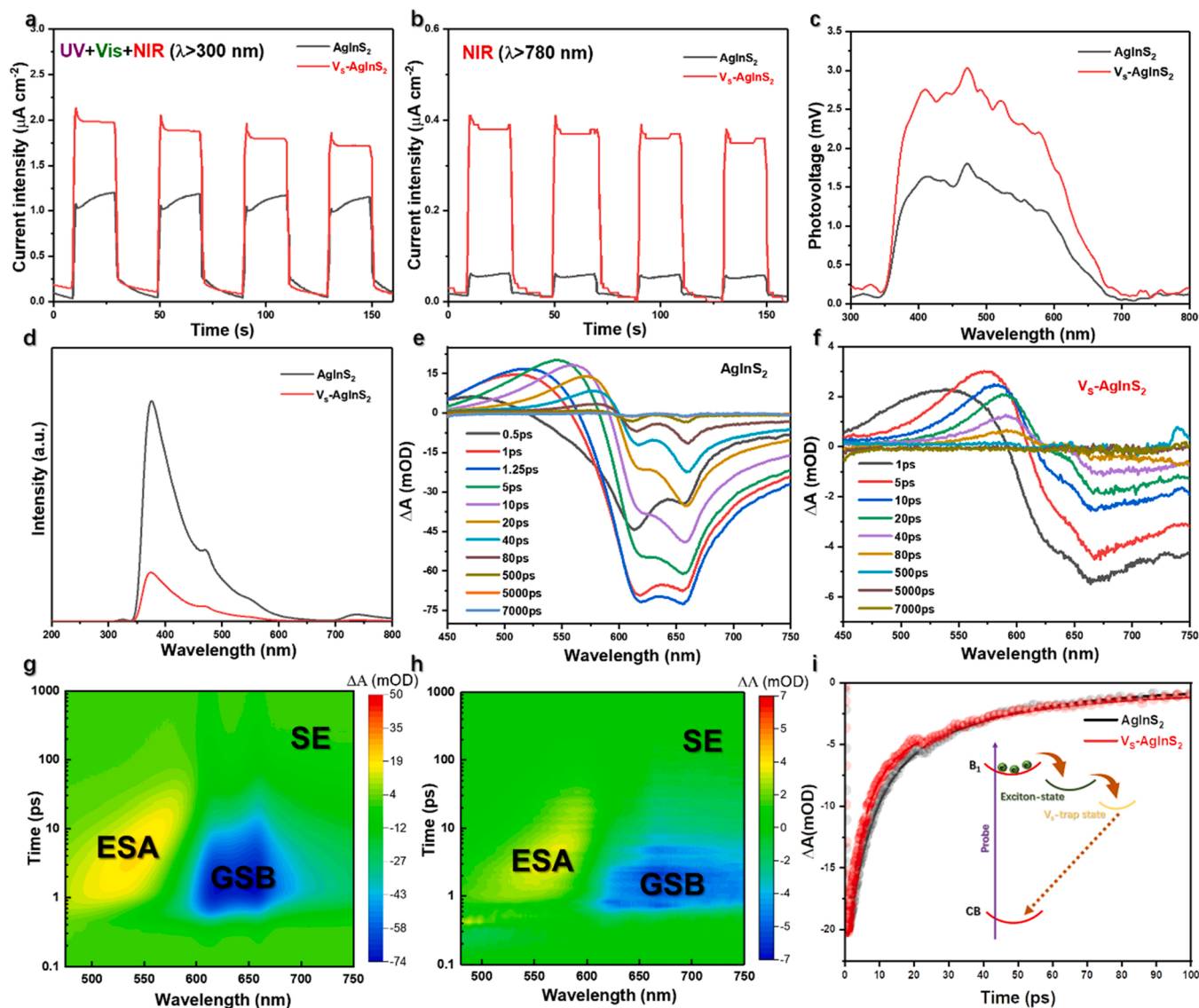


**Fig. 4.** Transient photocurrent over  $\text{AgInS}_2$  and  $\text{V}_5\text{-AgInS}_2$  under (a) full spectrum, (b) NIR light irradiation. (c) SPV spectra and (d) PL spectra over  $\text{AgInS}_2$  and  $\text{V}_5\text{-AgInS}_2$ . Transient absorption signals of (e)  $\text{AgInS}_2$  and (f)  $\text{V}_5\text{-AgInS}_2$  nanocrystal. 2D transient absorption surface plots of (g)  $\text{AgInS}_2$  and (h)  $\text{V}_5\text{-AgInS}_2$ . (i) The decay kinetics probed at 835 nm, and the inset shows the photophysical process of  $\text{V}_5\text{-AgInS}_2$ .

molecular contact,  $\text{CO}_2$  adsorption, and  $\text{CO}$  desorption processes of  $\text{AgInS}_2$  and  $\text{V}_5\text{-AgInS}_2$  nanocrystals are explored. From Fig. 5a, both samples display similar desorption peaks at about 510 K. However, for metallic  $\text{V}_5\text{-AgInS}_2$ , a visibly broader peak at 690 K is present, which might be due to  $\text{CO}_2$  desorption from the sulfur vacancy sites. The aforementioned interference is further supported by the  $\text{CO}_2$  adsorption isotherms (Fig. 5b), which exhibit apparently enhanced  $\text{CO}_2$  adsorption capacity of metallic  $\text{V}_5\text{-AgInS}_2$  resulting from its surface sulfur vacancies [50,51]. As displayed in Fig. S21, the BET surface area of  $\text{V}_5\text{-AgInS}_2$  was measured to be  $18.86 \text{ m}^2 \text{ g}^{-1}$ , which is higher than that of  $\text{AgInS}_2$  ( $5.30 \text{ m}^2 \text{ g}^{-1}$ ). From the  $\text{CO}$  temperature-programmed desorption (TPD) spectra of samples in Fig. 5c, the metallic  $\text{V}_5\text{-AgInS}_2$  sample exhibits a higher overall amount of  $\text{CO}$  desorption and lower desorption temperature according to the total intensity of peaks, revealing that the formed  $^*\text{CO}$  intermediates and gaseous  $\text{CO}$  can be released from the  $\text{V}_5\text{-AgInS}_2$  nanocrystals surface much easier. Furthermore, as displayed by the contact angle analysis (Fig. S22), metallic  $\text{V}_5\text{-AgInS}_2$  possesses a lower contact angle of  $59.8^\circ$  than that of the pristine  $\text{AgInS}_2$  ( $83.2^\circ$ ), indicating its higher surface hydrophilicity for water adsorption on their surfaces, and hence possibly aiding subsequent proton transfer to participate in

the  $\text{CO}_2$  RR.

To further verify the results of in situ DRIFTS analysis, Gibbs free energy calculations over these possible  $\text{CO}_2$  photoreduction pathways are carried out based on DFT study from constructed models (Fig. S23). As displayed in Figs. 5d and 5e, it is suggested that the formation of  $^*\text{COOH}$  is the rate-limiting step (Table S2) of  $\text{AgInS}_2$  and  $\text{V}_5\text{-AgInS}_2$  [52]. Under the circumstances, as revealed in Figs. 5d and 5e, the energy barrier for  $^*\text{CO}_2$  protonation to form  $^*\text{COOH}$  on pristine  $\text{AgInS}_2$  and  $\text{V}_5\text{-AgInS}_2$  (step schematic representation in Figs. S24 and S25) is 1.40 and 1.25 eV, respectively, indicating that  $\text{V}_5\text{-AgInS}_2$  is more likely to drive photocatalytic  $\text{CO}_2$  reduction, thus resulting in the high yield of  $\text{CO}$  and  $\text{CH}_4$  under full spectrum and visible light irradiation. Subsequently,  $^*\text{CO}$  protonation to  $^*\text{CHO}$  on pristine  $\text{AgInS}_2$  obtains an energy barrier of  $-0.17$  eV; Meanwhile,  $^*\text{CO}$  intermediate could transfer the gaseous  $\text{CO}$  spontaneously. Conversely, the  $\text{V}_5\text{-AgInS}_2$  had an energy barrier of 0.26 eV from  $^*\text{CO}$  protonation to  $^*\text{CHO}$ , which illustrates the reason for the high selectivity of  $\text{CO}$  over  $\text{V}_5\text{-AgInS}_2$  under NIR light illumination. More importantly, as exhibited by the charge difference distribution (Fig. 5f-g and S26), the  $^*\text{COOH}$  intermediates also tend to bond in Ag-In dual sites of  $\text{V}_5\text{-AgInS}_2$  nanocrystals, which perhaps helps



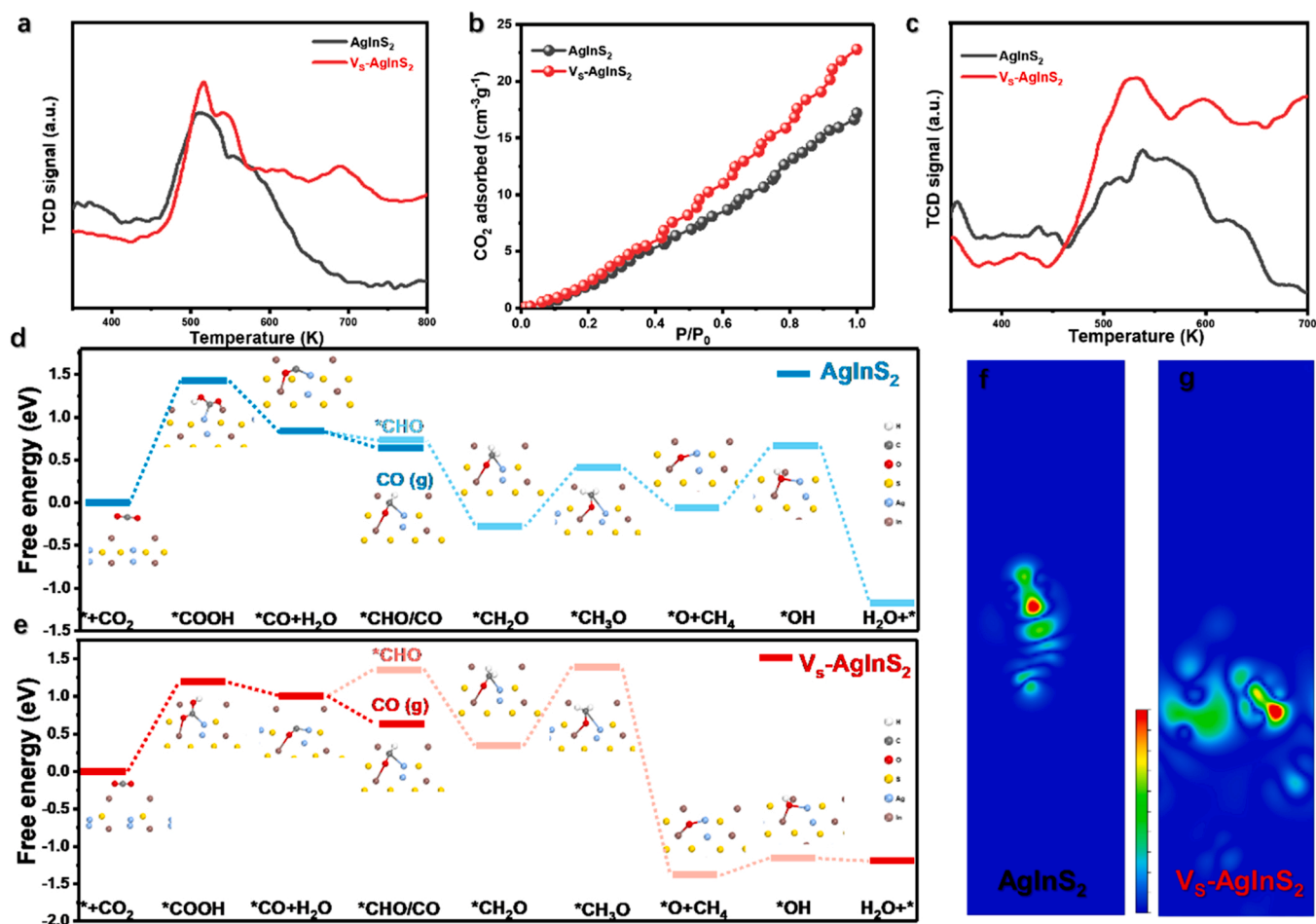


**Fig. 5.** (a) CO<sub>2</sub> TPD measurements, (b) CO<sub>2</sub> adsorption isotherms and (c) CO TPD measurements of AgInS<sub>2</sub> and VS-AgInS<sub>2</sub>. Free energy diagrams of CO<sub>2</sub> RR to CO and CH<sub>4</sub> over the (d) AgInS<sub>2</sub> and (e) VS-AgInS<sub>2</sub>, and the inset shows structural models of intermediates. Calculated electric charge density difference of (f) AgInS<sub>2</sub> and (g) VS-AgInS<sub>2</sub> in the step of \*COOH intermediate.

the following protonation step of CO<sub>2</sub> RR. Overall, VS-AgInS<sub>2</sub> possessed a better photocatalytic performance regardless of photocatalytic CO<sub>2</sub> reduction to CO under NIR light illumination.

#### 4. Conclusion

To our knowledge, this was the first study to realize NIR-driven CO<sub>2</sub> RR by designing vacancy-engineered metal sulfides with metallic characteristics. As an example, ternary metal chalcogenide, AgInS<sub>2</sub>, and carefully engineered sulfur vacated samples, metallic VS-AgInS<sub>2</sub>, were synthesized. UV-vis-NIR diffuse reflectance and fs-TAS analysis revealed that the presence of sulfur vacancies favored NIR light harvesting and promoted carrier separation. Moreover, in situ DRIFTS measurements and Gibbs free energy calculations together illustrated that the sulfur vacancies not only reduced the activation energy barrier of COOH\* but also prohibited the protonation step of CHO\*, thus resulting in CO formation instead of CH<sub>4</sub>. As a result, the metallic VS-AgInS<sub>2</sub> nanocrystals exhibited near 100% CO selectivity for IR light-driven CO<sub>2</sub> RR directly from the air. This work provided a straightforward path to accelerate the charge separation in defect-mediated metallic photocatalysts.

#### CRediT authorship contribution statement

**Kai Wang:** Experiment, Data processing & analysis, Writing – original draft, Revised manuscript preparation, Resources. **Haotian Qin, Qiang Cheng, Yanfang Zhu, Haiyan Hu, Jian Peng:** Investigation,

Data analysis. **Jun Li, Shuangqiang Chen:** Formal analysis, Writing – review & editing, Resources. **Guohong Wang, Shulei Chou and Shixue Dou:** Resources. **Yao Xiao:** Investigation, Formal analysis, Writing – review & editing, Resources.

#### Declaration of Competing Interest

The authors declare that they have no known competing financial interests or personal relationships that could have appeared to influence the work reported in this paper.

#### Data Availability

Data will be made available on request.

#### Acknowledgments

This work was supported by the National Natural Science Foundation of China (52104254, 52202284, 51971124, 52171217), Natural Science Foundation of Hubei Province (2021CFB242), Zhejiang Natural Science Foundation (LQ23E020002), WenZhou Natural Science Foundation (G20220019), Cooperation between industry and education project of Ministry of Education (220601318235513), State Key Laboratory of Electrical Insulation and Power Equipment, Xi'an Jiaotong University (EIPE22208). This study is dedicated to the 50th Anniversary of Hubei Normal University (HBNU).

## Appendix A. Supporting information

Supplementary data associated with this article can be found in the online version at [doi:10.1016/j.apcatb.2023.122763](https://doi.org/10.1016/j.apcatb.2023.122763).

## References

- [1] Y. Wang, Q. Zhou, Y. Zhu, D. Xu, Ultrathin High efficiency reduction of CO<sub>2</sub> to CO and CH<sub>4</sub> via photothermal synergistic catalysis of lead-free perovskite Cs<sub>3</sub>Sb<sub>2</sub>I<sub>9</sub>, *Appl. Catal. B* 294 (2021), 120236.
- [2] Z. Zhang, Y. Cao, F. Zhang, W. Li, Y. Li, H. Yu, M. Wang, H. Yu, Tungsten oxide quantum dots deposited onto ultrathin CdIn<sub>2</sub>S<sub>4</sub> nanosheets for efficient S-scheme photocatalytic CO<sub>2</sub> reduction via cascade charge transfer, *Chem. Eng. J.* 428 (2022), 131218.
- [3] D. Gao, W. Li, H. Wang, G. Wang, R. Cai, Heterogeneous catalysis for CO<sub>2</sub> conversion into chemicals and fuels, *Trans. Tianjin, Univ* 28 (2022) 245–264.
- [4] K. Feng, S. Wang, D. Zhang, L. Wang, Y. Yu, K. Feng, Z. Li, Z. Zhu, C. Li, M. Cai, Z. Wu, N. Kong, B. Yan, J. Zhong, X. Zhang, G.A. Ozin, L. He, Cobalt plasmonic superstructures enable almost 100% broadband photon efficient CO<sub>2</sub> photocatalysis, *Adv. Mater.* 32 (2020) 2000014.
- [5] L. Zhou, X. Zhang, L. Lin, P. Li, K. Shao, C. Li, T. He, Visible-light photocatalytic reduction of CO<sub>2</sub> by CoTe prepared via a template-free hydrothermal method, *Acta Phys.-Chim. Sin.* 33 (9) (2017) 1884–1890.
- [6] D. Song, H. Guo, K. Huang, H. Zhang, J. Chen, L. Wang, C. Lian, Y. Wang, Carboxylated carbon quantum dot-induced binary metal-organic framework nanosheet synthesis to boost the electrocatalytic performance, *Mater. Today* 54 (2022) 42–51.
- [7] Y. Xia, Z. Tian, T. Heil, A. Meng, B. Cheng, S. Cao, J. Yu, M. Antonietti, Highly selective CO<sub>2</sub> capture and its direct photochemical conversion on ordered 2D/1D heterojunctions, *Joule* 3 (2019) 1–14.
- [8] K. Wang, H. Wang, Q. Cheng, C. Gao, G. Wang, X. Wu, Molecular-functionalized engineering of porous carbon nitride nanosheets for wide-spectrum responsive solar fuel generation, *J. Colloid Interface Sci.* 607 (2022) 1061–1070.
- [9] L. Chen, T. Liu, S. Liu, S. Cai, X. Zou, J. Jiang, Z. Mei, G. Zhao, X. Yang, H. Guo, S vacant CuIn<sub>2</sub>S<sub>2</sub> confined in a few-layer MoSe<sub>2</sub> with interlayer expanded hollow heterostructures boost photocatalytic CO<sub>2</sub> reduction, *Rare Met* 41 (1) (2022) 144–154.
- [10] Z. Zhang, X. Liu, Y. Li, H. Yu, W. Li, H. Yu, Unveiling the role of Ag-Sb bimetallic S-scheme heterojunction for vis-NIR-light driven selective photoreduction CO<sub>2</sub> to CH<sub>4</sub>, *Appl. Catal. B* 319 (2022), 121960.
- [11] H. Ge, Y. Kuwahara, K. Kusu, Z. Bian, H. Yamashita, Ru/H<sub>2</sub>MoO<sub>3-y</sub> with plasmonic effect for boosting photothermal catalytic CO<sub>2</sub> methanation, *Appl. Catal. B* 317 (2022), 121734.
- [12] R. Feng, W. Lei, G. Liu, M. Liu, Visible- and NIR-light responsive black-phosphorus based nanostructures in solar fuel production and environmental remediation, *Adv. Mater.* 30 (2018) 1804770.
- [13] K. Wang, X. Feng, Y. Shanguan, X. Wu, H. Chen, Selective CO<sub>2</sub> photoreduction to CH<sub>4</sub> mediated by dimension matched 2D/2D Bi<sub>3</sub>NbO<sub>7</sub>/g-C<sub>3</sub>N<sub>4</sub> S-scheme heterojunction, *Chin. J. Catal.* 43 (2022) 246–254.
- [14] J. Hu, L. Yu, J. Deng, Y. Wang, K. Cheng, C. Ma, Q. Zhang, W. Wen, S. Yu, Y. Pan, J. Yang, H. Ma, F. Qi, Y. Wang, Y. Zheng, M. Chen, R. Huang, S. Zhang, Z. Zhao, J. Mao, X. Meng, Q. Ji, G. Hou, X. Han, X. Bao, Y. Wang, D. Deng, Sulfur vacancy-rich MoS<sub>2</sub> as a catalyst for the hydrogenation of CO<sub>2</sub> to methanol, *Nat. Catal.* 4 (3) (2021) 242–250.
- [15] K. Wang, Q. Wang, K. Zhang, G. Wang, H. Wang, Selective solar-driven CO<sub>2</sub> reduction mediated by 2D/2D Bi<sub>2</sub>O<sub>3</sub>/SiO<sub>2</sub>/MXene nanosheets heterojunction, *J. Mater. Sci. Technol.* 124 (2022) 202–208.
- [16] Y. Han, B. Tang, L. Wang, H. Bao, Y. Lu, C. Guan, L. Zhang, M. Le, Z. Liu, M. Wu, Machine learning driven synthesis of carbon dots with enhanced quantum yield, *ACS Nano* 14 (2020) 14761–14768.
- [17] L. Tan, S. Xu, Z. Wang, Y. Xu, X. Wang, X. Hao, S. Bai, C. Ning, Y. Wang, W. Zhang, Y. Jo, S. Hwang, X. Cao, X. Zheng, H. Yan, Y. Zhao, H. Duan, Y. Song, Highly selective photoreduction of CO<sub>2</sub> with suppressing H<sub>2</sub> evolution over monolayer layered double hydroxide under irradiation above 600 nm, *Angew. Chem. Int. Ed.* 58 (2019) 2–10.
- [18] Y. Zhao, G. Chen, T. Bian, C. Zhou, G. Waterhouse, L. Wu, C.H. Tung, L.J. Smith, D. O'Hare, T. Zhang, Defect-rich ultrathin ZnAl-layered double hydroxide nanosheets for efficient photoreduction of CO<sub>2</sub> to CO with water, *Adv. Mater.* 27 (2015) 7824–7831.
- [19] K. Wang, Y. Du, Y. Li, X. Wu, H. Hu, G. Wang, Y. Xiao, S. Chou, G. Zhang, Atomic-level insight of sulfidation-engineered Aurivillius-related Bi<sub>2</sub>O<sub>3</sub>/SiO<sub>2</sub> nanosheets enabling visible light low-concentration CO<sub>2</sub> conversion, *Carbon Energy* (2022), <https://doi.org/10.1002/cey.2.264>.
- [20] S. Wu, J. Wang, Q. Li, Z. Huang, Z. Rao, Y. Zhou, Bi/BiOCl nanosheets enriched with oxygen vacancies to enhance photocatalytic CO<sub>2</sub> reduction, *Trans. Tianjin, Univ* 27 (2021) 155–164.
- [21] K. Wang, L. Jiang, X. Wu, G. Zhang, Vacancy mediated Z-scheme charge transfer in a 2D/2D La<sub>2</sub>Ti<sub>2</sub>O<sub>7</sub>/g-C<sub>3</sub>N<sub>4</sub> nanojunction as a bifunctional photocatalyst for solar-to-energy conversion, *J. Mater. Chem. A* 8 (2020) 13241–13247.
- [22] R. Niu, Q. Liu, B. Huang, Z. Liu, W. Zhang, Z. Peng, Z. Wang, Y. Yang, Z. Gu, J. Li, Black phosphorus/Bi<sub>19</sub>Br<sub>3</sub>S<sub>27</sub> van der Waals heterojunctions ensure the supply of activated hydrogen for effective CO<sub>2</sub> photoreduction, *Appl. Catal. B* 317 (2022), 121727.
- [23] C. Bie, B. Zhu, F. Xu, L. Zhang, J. Yu, In situ grown monolayer N-doped graphene on CdS hollow spheres with seamless contact for photocatalytic CO<sub>2</sub> reduction, *Adv. Mater.* 31 (2019) 1902868.
- [24] Q. Sun, J. Xu, F. Tao, W. Ye, C. Zhou, J. He, J. Lu, Boosted inner surface charge transfer in perovskite nanodots@mesoporous titania frameworks for efficient and selective photocatalytic CO<sub>2</sub> reduction to methane, *Angew. Chem. Int. Ed.* 61 (2022), e202200872.
- [25] J. Xu, Z. Ju, W. Zhang, Y. Pan, J. Zhu, J. Mao, X. Zheng, H. Fu, M. Yuan, H. Chen, R. Li, Efficient infrared-light-driven CO<sub>2</sub> reduction Over ultrathin metallic Ni-doped CoS<sub>2</sub> nanosheets, *Angew. Chem. Int. Ed.* 60 (2021) 8705–8709.
- [26] F. You, J. Wan, J. Qi, D. Mao, N. Yang, Q. Zhang, L. Gu, D. Wang, Lattice distortion in hollow multi-shelled structures for efficient visible light CO<sub>2</sub> reduction with a SnS<sub>2</sub>/SnO<sub>2</sub> junction, *Angew. Chem. Int. Ed.* 58 (2019) 1–5.
- [27] J. Li, W. Pan, Q. Liu, Z. Chen, Z. Chen, X. Feng, H. Chen, Interfacial engineering of Bi<sub>19</sub>Br<sub>3</sub>S<sub>27</sub> nanowires promotes metallic photocatalytic CO<sub>2</sub> reduction activity under near-infrared light irradiation, *J. Am. Chem. Soc.* 143 (2021) 6551–6559.
- [28] X. Li, L. Liang, Y. Sun, J. Xu, X. Jiao, X. Xu, H. Ju, Y. Pan, J. Zhu, Y. Xie, Ultrathin conductor enabling efficient IR light CO<sub>2</sub> reduction, *J. Am. Chem. Soc.* 141 (2019) 423–430.
- [29] C. Zhan, B. Liu, Y. Huang, S. Hu, B. Ren, M. Moskovits, Z. Tian, Disentangling charge carrier from photothermal effects in plasmonic metal nanostructures, *Nat. Commun.* 10 (2019) 2671.
- [30] C. Du, B. Yan, G. Yang, Self-integrated effects of 2D ZnIn<sub>2</sub>S<sub>4</sub> and amorphous Mo<sub>2</sub>C nanoparticles composite for promoting solar hydrogen generation, *Nano Energy* 76 (2020), 105031.
- [31] X. Li, Y. Sun, J. Xu, Y. Shao, J. Wu, X. Xu, Y. Pan, H. Ju, J. Zhu, Y. Xie, Selective visible-light-driven photocatalytic CO<sub>2</sub> reduction to CH<sub>4</sub> mediated by atomically thin CuIn<sub>2</sub>S<sub>2</sub> layers, *Nat. Energy* 4 (2019) 690–699.
- [32] Q. Cheng, K. Kang, Y. Li, J. Wang, Z. Wang, D. Selishchev, X. Wang, G. Zhang, Achieving efficient toluene mineralization over ordered porous LaMnO<sub>3</sub> catalyst: The synergistic effect of high valence manganese and surface lattice oxygen, *Appl. Surf. Sci.* 615 (2023), 156248.
- [33] J. Di, C. Zhu, M. Ji, M. Duan, R. Long, C. Yan, K. Gu, J. Xiong, Y. She, J. Xia, H. Li, Z. Liu, Defect-rich Bi<sub>12</sub>O<sub>17</sub>C<sub>12</sub> nanotubes self-accelerating charge separation for boosting photocatalytic CO<sub>2</sub> reduction, *Angew. Chem. Int. Ed.* 57 (2018) 14847–14851.
- [34] A. Meng, B. Cheng, H. Tan, J. Fan, C. Su, J. Yu, TiO<sub>2</sub>/polydopamine S-scheme heterojunction photocatalyst with enhanced CO<sub>2</sub>-reduction selectivity, *Appl. Catal. B* 289 (2021), 120039.
- [35] H. Huang, R. Shi, Z. Li, J. Zhao, C. Su, T. Zhang, Triphase photocatalytic CO<sub>2</sub> reduction over silver-decorated titanium oxide at a gas-water boundary, *Angew. Chem. Int. Ed.* 61 (2022), e202200802.
- [36] Q. Cheng, Y. Li, Z. Wang, X. Wang, G. Zhang, Boosting full-spectrum light driven surface lattice oxygen activation of ZnMn<sub>2</sub>O<sub>4</sub> by facet engineering for highly efficient photothermal mineralization of toluene, *Appl. Catal. B* 324 (2023), 122274.
- [37] Z. Zhao, D. Wang, R. Gao, G. Wen, M. Feng, G. Song, J. Zhu, D. Luo, H. Tan, X. Ge, W. Zhang, Y. Zhang, L. Zheng, H. Li, Z. Chen, Magnetic-field-stimulated efficient photocatalytic N<sub>2</sub> fixation over defective BaTiO<sub>3</sub> perovskites, *Angew. Chem.* 133 (2021) 2–11.
- [38] X. Zhang, J. Liu, H. Zhang, Z. Wan, J. Li, Uncovering the pathway of peroxymonosulfate activation over Co<sub>0.5</sub>Zn<sub>0.5</sub>O nanosheets for singlet oxygen generation: Performance and membrane application, *Appl. Catal. B* 327 (2023), 122429.
- [39] K. Wang, L. Peng, X. Shao, Q. Cheng, J. Wang, K. Li, H. Wang, Nb–O–C charge transfer bridge in 2D/2D Nb<sub>2</sub>O<sub>5</sub>/g-C<sub>3</sub>N<sub>4</sub> S-scheme heterojunction for boosting solar-driven CO<sub>2</sub> reduction: In situ illuminated X-ray photoelectron spectroscopy investigation and mechanism insight, *Sol. RRL* (2022) 2200434.
- [40] Q. Cheng, Z. Wang, X. Wang, J. Li, Y. Li, G. Zhang, A novel Cu<sub>1.5</sub>Mn<sub>1.5</sub>O<sub>4</sub> photothermal catalyst with boosted surface lattice oxygen activation for efficiently photothermal mineralization of toluene, *Nano Res* (2022), <https://doi.org/10.1007/s12274-022-4946-6>.
- [41] L. Liu, S. Wang, H. Huang, Y. Zhang, T. Ma, Surface sites engineering on semiconductors to boost photocatalytic CO<sub>2</sub> reduction, *Nano Energy* 75 (2020), 104959.
- [42] Z. Hu, T. Chen, Z. Xie, C. Guo, W. Jiang, Y. Chen, Y. Xu, Emission tunable AgInS<sub>2</sub> quantum dots synthesized via microwave method for white light-emitting diodes application, *Opt. Mater.* 124 (2022), 111975.
- [43] A. Hirase, Y. Hamaoka, T. Kuzuya, Ligand-induced luminescence transformation in AgInS<sub>2</sub> nanoparticles: From defect emission to band-edge emission, *J. Phys. Chem. Lett.* 11 (2020) 3969–3974.
- [44] S. Song, Z. Liang, W. Fu, T. Peng, Preparation of single-crystalline AgInS<sub>2</sub> octahedrons with exposed {111} facets and its visible-light-responsive photocatalytic H<sub>2</sub> production activity, *ACS Appl. Mater. Interfaces* 9 (2017) 17013–17023.
- [45] J. Qin, X. Hu, X. Li, Z. Yin, B. Liu, K. Lam, 0D/2D AgInS<sub>2</sub>/MXene Z-scheme heterojunction nanosheets for improved ammonia photosynthesis of N<sub>2</sub>, *Nano Energy* 61 (2019) 27–35.
- [46] K. Wang, X. Shao, K. Zhang, J. Wang, X. Wu, H. Wang, 0D/3D Bi<sub>3</sub>TaO<sub>7</sub>/ZnIn<sub>2</sub>S<sub>4</sub> heterojunction photocatalyst towards degradation of antibiotics coupled with simultaneous H<sub>2</sub> evolution: In situ irradiated XPS investigation and S-scheme mechanism insight, *Appl. Surf. Sci.* 596 (2022), 153444.
- [47] H. Cao, J. Xue, Z. Wang, J. Dong, W. Li, R. Wang, S. Sun, C. Gao, Y. Tan, X. Zhu, J. Bao, Construction of atomically dispersed Cu sites and S vacancies on CdS for enhanced photocatalytic CO<sub>2</sub> Reduct., *J. Mater. Chem. A* 9 (2021) 16339–16344.



- [48] X. Wu, W. Zhang, J. Li, Q. Xiang, Z. Liu, B. Liu, Identification of the active sites on metallic  $\text{MoO}_{2-x}$  nano-seaurchin for atmospheric  $\text{CO}_2$  photoreduction under UV, visible, and near-infrared light illumination, *Angew. Chem. Int. Ed.* (2022), e202213124.
- [49] C. Bie, B. Zhu, L. Wang, H. Yu, C. Jiang, T. Chen, J. Yu, A bifunctional  $\text{CdS}/\text{MoO}_2/\text{MoS}_2$  catalyst enhances photocatalytic  $\text{H}_2$  evolution and pyruvic acid synthesis, *Angew. Chem. Int. Ed.* 61 (2022), e202212045.
- [50] K. Wang, X. Shao, Q. Cheng, K. Li, X. Le, G. Wang, H. Wang, In situ-illuminated X-ray photoelectron spectroscopy investigation of S-scheme  $\text{Ta}_2\text{O}_5/\text{ZnIn}_2\text{S}_4$  core-shell hybrid nanofibers for highly efficient solar-driven  $\text{CO}_2$  overall splitting, *Sol. RRL* (2022) 2200736.
- [51] K. Wang, H. Qin, X. Shao, L. Jiang, K. Li, J. Wang, L. Zhou, Q. Cheng, G. Wang, H. Wang, Unveiling S-scheme charge transfer pathways in  $\text{In}_2\text{S}_3/\text{Nb}_2\text{O}_5$  hybrid nanofiber photocatalysts for low-concentration  $\text{CO}_2$  hydrogenation, *Sol. RRL* (2022) 2200963.
- [52] J. Di, C. Chen, S. Yang, S. Chen, M. Duan, J. Xiong, C. Zhu, R. Long, W. Hao, Z. Chi, H. Chen, Y. Weng, J. Xia, L. Song, S. Li, H. Li, Z. Liu, Isolated single atom cobalt in  $\text{Bi}_3\text{O}_4\text{Br}$  atomic layers to trigger efficient  $\text{CO}_2$  photoreduction, *Nat. Commun.* 10 (2019) 2840.